DEVELOPMENT OF AN ORTHOGONAL DOUBLE-IMAGE PROCESSING ALGORITHM TO MEASURE BUBBLE VOLUME IN A TWO-PHASE FLOW

SEONG-JIN KIM and GOON-CHERL PARK*
Nuclear thermal hydraulics engineering laboratory, Department of Nuclear Engineering, Seoul National University,
San 56-1, Sillim-dong, Kwanak-gu, Seoul, 151-742, Korea
*Corresponding author. E-mail : parkgc@snu.ac.kr

Received December 14, 2006
Accepted for Publication July 6, 2007

In this paper, an algorithm to reconstruct two orthogonal images into a three-dimensional image is developed in order to measure the bubble size and volume in a two-phase boiling flow. The central-active contour model originally proposed by P. Szczypiński and P. Strumiłło is modified to reduce the dependence on the initial reference point and to increase the contour stability. The modified model is then applied to the algorithm to extract the object boundary. This improved central contour model could be applied to obscure objects using a variable threshold value. The extracted boundaries from each image are merged into a three-dimensional image through the developed algorithm. It is shown that the object reconstructed using the developed algorithm is very similar or identical to the real object. Various values such as volume and surface area are calculated for the reconstructed images and the developed algorithm is qualitatively verified using real images from rubber clay experiments and quantitatively verified by simulation using imaginary images. Finally, the developed algorithm is applied to measure the size and volume of vapor bubbles condensing in a subcooled boiling flow.

KEYWORDS : Active Contour Model, Central Contour Model, SNAKE, Variable Threshold Level, Volume, Equivalent Diameter, Subcooled Boiling

1. INTRODUCTION

Digital image processing (DIP) has garnered research attention as a means to analyze two-phase flows such as subcooled boiling phenomena. In particular, many studies on the measurement of the bubble size have conducted modeling involving DIP with high speed camera techniques [1,2]. In previous studies, images taken in one direction of objects were considered to be axis-symmetric, such as a spheroid, in order to calculate the volume or equivalent diameter. However, since most objects have three-dimensional degrees of freedom, one-directional image processing is limited in its capacity to precisely simulate the object.

An orthogonal double-image was used to analyze bubble size and volume by Zeitoun et al. [3]. They divided the bubbles into two groups: spherical and elongated. In the former, the bubble volume and surface area are calculated by rotating a cross-section around the maximum diameter and by averaging the values on the orthogonal double-image. In the latter, each image is divided into six slices and the upper and bottom sections are assumed to be spherical domes and the inner sections to be parts of conical bodies whose two bases are assumed to be ellipses. However, there is no method to determine the bubble boundary in their research, thus necessitating a complicated process to calculate the surface area and volume in an elongated bubble.

Recently, Hibiki et al. [4] and Takamasa et al. [5] applied an image processing algorithm used by Takamasa and Watarai [6] and a stereo image-processing method (SIM) in order to obtain dimensions of bubbles such as major and minor axes. They assumed that the bubble is a triaxial ellipsoid and they determined the dimensions of three axes from an analysis of two simultaneous images taken from orthogonal directions. However, assumptions of an ellipsoidal bubble shape can be insufficient to express deformed bubbles from a triaxial ellipsoid.

One of the initial and fundamental stages of DIP is the detection of characteristic image regions in order to decompose images into objects of interest and their background, and the image edges are used as characteristic regions. The most commonly used edge finding techniques are the gradient based Prewitt, Sobel, and Laplace detectors [7], the second derivative zero-crossing detector [8], and a computational approach based on the Canny criteria [9]. However, these edge finding techniques fail in producing confident results due to noise, image blur, and non-uniform scene illumination. Also, continuous image

boundaries such as moving bubbles may cause broken edge fragments or may not be detected at all. To overcome these defects, an active contour model has been used as an edge detecting method. The active contour is an energy-minimizing curve that deforms to fit image features, known as snakes, and was first proposed by Kass [10]. This energy depends on its shape and location within the image and then local minima of this energy correspond to desired image properties. The active contour model has meanwhile become an established and important technique for locating image boundaries in computer vision applications. Recently, a number of papers related to this subject have been published and some improvements and extensions to the original method have been reported [11,12].

In the present paper, to overcome the limitations of one-directional image processing, a simple algorithm is developed using two images for the same object in an orthogonal direction. The main structure of the algorithm based on an active contour model is reconstruction into three-dimensional objects from two images. In order to distinguish the object of interest from the background, an active contour model is applied and modified. The developed two-directional image processing approach is applied to virtual bubble images and is verified by simulation using imaginary images. Finally, the developed algorithm is applied to measure the size and volume of condensed vapor bubbles in subcooled flow boiling.

2. DESCRIPTION OF THE CENTRAL CONTOUR MODEL

In order to measure the bubble size and volume from the images, the boundaries between the backgrounds and bubbles should be discriminated, i.e., extraction of bubble edges should be preceded. The active contour model is used to decompose or segment visual information into the object of interest and its background,

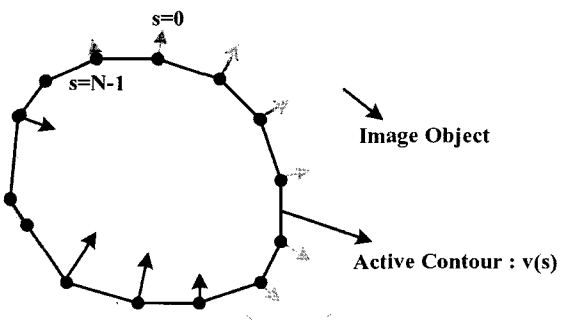

Fig. 1.Construction of an Active Contour Model

according to the snake model first proposed by Kass [10]. The snake is an energy-minimizing spline guided by external constraint forces and influenced by image forces that pull it toward features such as lines and edges. Figure 1 shows the concept of the snake, where the arrows represent the moving directions of the snake's points towards the borders of the object to be analyzed when the contour consists of a set of N-points. The proposed energy function is given by the following integral equation:

$$E_{snake} = \int_0^{S_m} \left[E_{int}(v(s)) + E_{ext}(v(s)) + E_{image}(v(s)) \right] ds \qquad (1)$$

The position of the snake is described parametrically by $v(s) = (x(s), y(s))$, where $x(s)$ and $y(s)$ are x- and y-coordinates along the contour. s is a parameter variable to describe the contour and is from the first to the last point comprising the contour. That is, $s=0$ and $s=S_m$ denote the first and last point of the contour. E_{int} represents the internal potential energy of the contour, E_{ext} the energy that models external constraints imposed onto the contour shape, and E_{image} the energy derived from image features, such as the image brightness distribution. In this paper, the central contour model proposed by P. Szczypiński and P. Strumiłło [13] is used to extract the boundary edges. The central contour model to find the boundary is briefly described below.

This approach is based on the idea that the initial potential energy of contour E_{snake} is minimized using a technique in which a lower contour energy state is reached by converting its potential energy to kinetic energy and then dissipating this kinetic energy through an energy dissipating function. This means that a certain mass is associated with the moving contour, which dissipates its kinetic energy due to the presence of some viscosity of an abstract environment in contour motions. Thus, the equation of the contour motion to describe the contour dynamics is given as:

$$m\frac{\partial^2 v(s,t)}{\partial t^2} + \gamma\frac{\partial v(s,t)}{\partial t} = \vec{F} \qquad (2)$$

where m is the virtual mass density of the contour, γ the virtual damping viscosity factor, which accounts for the contour energy dissipation, and $\vec{F}$ the intrinsic and external forces acting on the contour. Instead of a continuous contour line, a set of points is used to discretize spaces and the time domain is discretized to numbered time instances. The discrete equation of Eq. (2) is assumed as:

$$m\frac{v(s,t)-2v(s,t-1)+v(s,t-2)}{1^2} + \gamma\frac{v(s,t)-v(s,t-1)}{1} = \vec{F}(t-1) \qquad (3)$$

$$\vec{F} = \vec{F}_{ext} + \vec{F}_{tens} + \vec{F}_{rig} + \vec{F}_{img} \quad (4)$$

where $\vec{F}_{ext}$ is the force minimizing the snake energy component E_{ext} in Eq. (1). $\vec{F}_{tens}$ and $\vec{F}_{rig}$ are the forces resulting from the contour tension and rigidity, respectively, associated with the contour internal energy (E_{int}), and $\vec{F}_{img}$ is the force vector derived from the image brightness distribution designed to attract the contour to the image's salient features.

The discrete equation to find the contour coordinated for the current time t from Eqs. (3) and (4) is:

$$v(s,t) = \frac{2mv(s,t-1) - mv(s,t-2) + \gamma v(s,t-1) + \left[\vec{F}_{ext} + \vec{F}_{tens} + \vec{F}_{rig} + \vec{F}_{img}\right]_{t-1}}{m+\gamma} \quad (5)$$

where the discrete equations for the forces have been proposed [7] as follows:

$$\vec{F}_{ext}(s,t) = \left[3h_2\{r(s,t)\}^2 - \frac{h_1}{r(s,t)}\right]\left[\frac{x-x_0}{r(s,t)}, \frac{y-y_0}{r(s,t)}\right]^T \quad (6)$$

$$\vec{F}_{tens}(s,t) = W_1\left[\frac{v(s+1)+v(s-1)}{2} - v(s)\right] \quad (7)$$

$$\vec{F}_{rig}(s,t) = W_2\left[\frac{v(s+2)+v(s-2)-4\{v(s+1)+v(s-1)\}}{6} + v(s)\right] \quad (8)$$

$$\vec{F}_{img}(s,t) = J_W\left[J(v(s,t)) - J_C\right]\left[\frac{x-x_0}{r(s,t)}, \frac{y-y_0}{r(s,t)}\right]^T \quad (9)$$

where $r(s)$ is the distance between the points belonging to the contour and an arbitrarily chosen reference point encircled by the contour calculated as $r(s) = \sqrt{(x-x_0)^2 + (y-y_0)^2}$.

The force $\vec{F}_{ext}$ is represented as the derivative of the energy function E_{ext} with respect to the distance between contour snake points and an arbitrarily chosen reference point encircled by the contour, i.e. $\vec{F}_{ext} = \partial E_{ext} / \partial s$, in P. Szczypiński and P. Strumiłło's research. They represented the energy function as $E_{ext}(r(s)) = -h_1 \ln(r(s)) + h_2 r^3(s)$. The forces, $\vec{F}_{tens}$ and $\vec{F}_{rig}$, which associate with contour internal energy E_{int}, are derived via the following equation:

$$E_{int}(v(s)) = 2w_1\left|\frac{\partial v(s)}{\partial s}\right|^2 + 2w_2\left|\frac{\partial^2 v(s)}{\partial s^2}\right|^2 = 2w_1 E_{tens} + 2w_2 E_{rig} \quad (10)$$

where w_1 and w_2 regulate the contour tension energy E_{tens} and the contour rigidity energy E_{rig}, respectively. E_{tens} and E_{rig} denote the contour's resistance to stretching and to bending, respectively. For a chosen snake point s, the contour tension energy $E_{tens}(v(S))$ can be considered as $w_1[v(s)-v(s-1)]^2 + w_1[v(s+1)-v(s)]^2$ due to the influences of adjacent snake points, i.e. $v(s-1)$ and $v(s+1)$. This energy reaches a minimum (i.e. $\partial E_{tens} / \partial s = 0$) for $v(s) = [v(s+1) + v(s-1)]/2$ as given by Eq. (7). For the rigidity force, $\partial^2 E_{rig} / \partial s^2$ becomes zero for $v(s) = [v(s+1) + v(s-1)]/2$ to similarly reach minimum rigidity energy. Finally, the rigidity force is derived as given by Eq. (8). For the image force $\vec{F}_{img}$, they assumed some threshold value between the object of interest and the background brightness and delineated this with Eq. (9).

At this time, use of the reference point encircled by the contour is advantageous in finding a boundary due to the presence of pre-information for the boundary. However, it also has a disadvantage in that the determined boundary according to the position of the initially referred point may be erroneous due to the dependency of the model equations. In Eq. (9), $J(v(s,t))$ denotes the gray value at $v(s,t)$ and the used image is a pixel type rather than a vector type. Thus, the image has a local gray value only at an integer lattice and the discrete gray value may generate unstable contours. This confirms the need for interpolations or image functions between the integer points of the image.

The meanings of the parameters in Eqs. (6) to (9) are described in Table 1. The range of the values has been presented in P. Szczypiński and P. Strumiłło's research and the indicated values are used in this study. In Table 1, the parameter of the threshold level, J_C, plays an important role of moving the contour to the boundary. The central contour model uses a constant threshold level, and hence the method of locating the boundary may fail when the object's surrounding are misty or opaque. Therefore, a method of variable or smart threshold value detection is needed. Thus, the central-active contour model proposed by P. Szczypiński and P. Strumiłło does not perform well when the contrast value on the object's boundary is not uniform; for example, a silhouette of a transparent object such as the bubbles shown in Fig. 2. Figure 2 shows bubbles in a subcooled boiling flow at atmospheric pressure. Note that the bubbles have specular points due to reflected and refracted rays from other bubbles. In such as case as this, the gray levels on the boundary of a single bubble are locally different, which necessitates the application of a local threshold level.

3. MODIFICATION OF THE CENTRAL CONTOUR MODEL

In the previous section, the central contour model to be used in this study was explained and aspects for improvement were itemized in order to obtain a more distinct and stable boundary that is independent of the

Table 1. A Set of Model Parameters

Parameter Name	Value	Description
Tension (W_1)	0.625	Regulates contour tension energy (Resistance to stretching)
Rigidity (W_2)	0.0625	Regulates contour rigidity energy (Resistance to bending)
Viscosity (γ)	360	Damping viscosity factor accounting for contour energy dissipation
Mass (m)	0.1	The mass density of the contour
Contrast coefficient (J_w)	-2	The coefficient defining the magnitude and direction of image force
Coefficient (h_1)	0.1719	Energy function coefficient 1.
Coefficient (h_2)	0.004	Energy function coefficient 2.
Threshold level (J_c)	variable	Threshold brightness value

Fig. 2. Bubble Image in Subcooled Boiling Flow

initial reference point. The suggestions for improvement are summarized as follows:

i. Area-weighted centroid to reduce dependency on the reference point
ii. Bilinear interpolation to increase the stability for the force on the image due to the pixel images
iii. Variable local threshold value to extract obscure boundaries

3.1 Area-Weighted Centroid

The initial reference point is fixed until the completion of the calculation, and as such the result may be affected by the choice of this point. Thus, the reference point must be updated every iteration even if the positions of the reference point correspond with the case of using a different reference point. The reference point is improved using an area-weighted centroid. Figure 3 shows the area-weighted

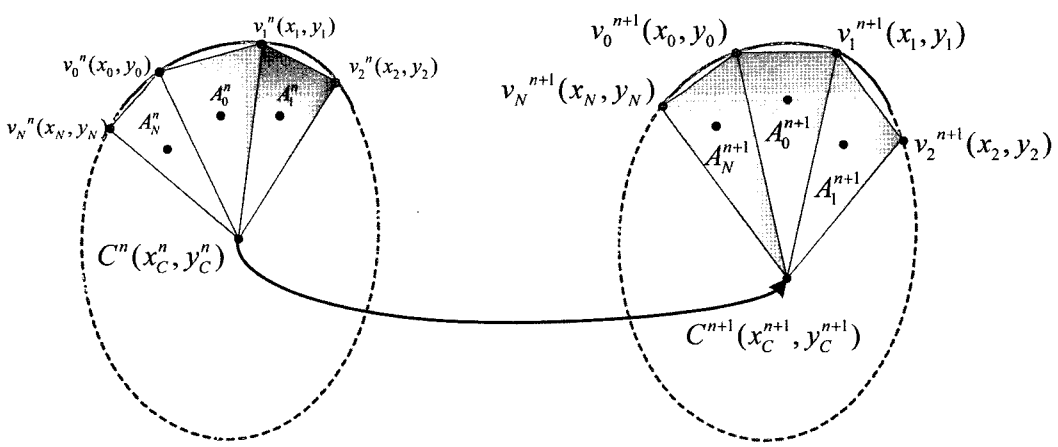

Fig. 3. Area-Weighted Centroid

centroid. The initial reference point is selected arbitrarily in the same manner as in the original central contour model. This point is then used to calculate the first contour through the first iteration. The reference point is subsequently updated as the area-weighted centroid, and the calculated centroid is used as the reference point at the next iteration. The area-weighted centroid, (x_c,y_c), is calculated as follows:

$$x_c^{(n+1)} = \frac{1}{\sum_{i=0}^{N} A_i^{(n)}} \left[\sum_{i=0}^{N} \left(\frac{x_c^{(n)} + x_i^{(n)} + x_{i+1}^{(n)}}{3} \right) A_i^{(n)} \right] \quad (11.a)$$

$$y_c^{(n+1)} = \frac{1}{\sum_{i=0}^{N} A_i^{(n)}} \left[\sum_{i=0}^{N} \left(\frac{y_c^{(n)} + y_i^{(n)} + y_{i+1}^{(n)}}{3} \right) A_i^{(n)} \right] \quad (11.b)$$

where $A_i^{(n)}$ denotes the i^{th} triangle area that is connected among the previous centroid, the i^{th}, and $(i+1)^{th}$ contour points at the n step. In the improved central contour model, the initially referred point is used at the beginning, but the effects of the initially referred point decrease with further iterations.

3.2 Bilinear Interpolation

In Eq. (9), $J(v(s,t))$ indicates the gray value at $v(s,t)$ and the used image is a pixel type rather than a vector type. Since the image has a local gray value only at an integer lattice and the discrete gray value may generate instability of contours, bilinear interpolation is used to ensure stability of the force on the image due to the pixel images. Figure 4 shows this bilinear interpolation, which is given as follows:

$$\begin{aligned} J(v(s,t)) = {} & u_x u_y J_{i+1,j+1} + (1-u_x)(1-u_y) J_{i,j} \\ & + u_x (1-u_y) J_{i+1,j} + (1-u_x) u_y J_{i,j+1} \end{aligned} \quad (12)$$

where u_x and u_y are the x- and y-directional ratios between the considered point and the near integer lattice point, respectively.

3.3 Variable Local Threshold Value

When the contrast value on an object's boundary is not uniform, a local threshold level needs to be applied using the original central contour model. First, in order to find the local threshold level, the image domain needs to be divided into sub-domains, which serve to exclude unnecessary image regions. The division of sub-domains might affect the calculation efficiency for determining the conversed solutions, i.e., the extraction of an actual boundary, and should be changed whenever the contour moves. To satisfy these conditions, a dual-active contour model is used. The dual technique uses an internal and external contour as the initial snakes [14]. This approach basically consists of comparing one contour that expands from inside the target feature with another that contracts from the outside. The two contours are interlinked to provide an adequate "driving force" that pushes out the contours of the local minima, thus making the solution less sensitive to the initial position, as shown in Fig. 5.

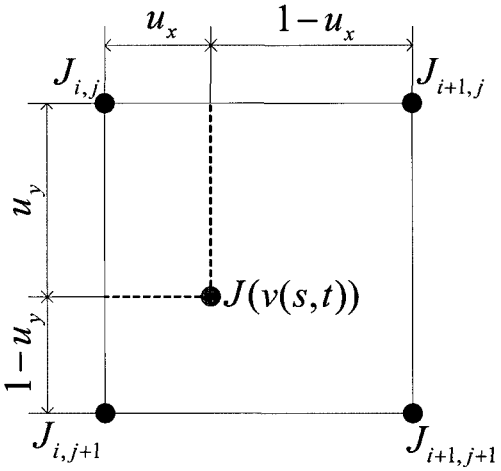

Fig. 4. Bilinear Interpolation

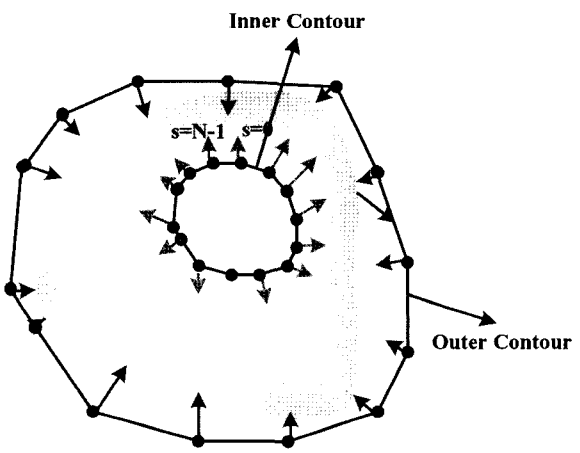

Fig. 5. Construction of Dual Active Contour Model

In this study, the driving force between the inner and outer contours is used to constrain the alignment of the three points. That is, the center point in the central-active

contour model, the m[th] point on the inner contour, and the m[th] point on the outer contour are aligned to the same line by using the driving force, as shown in Fig. 6. Figure 6 illustrates the iterative threshold method between the inner and outer contours. The iterative threshold method is one means of finding the threshold level in the images. The following explains the iterative threshold level.

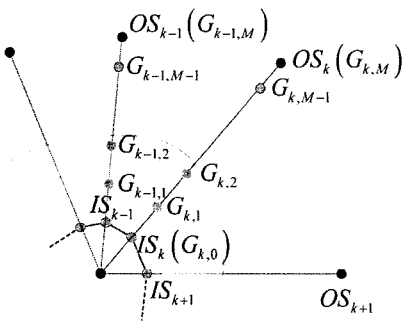

Fig. 6. Inner and Outer Contour to Apply the Iterative Threshold Method

First, an initial threshold level, $\mu^{(0)}$, is estimated by calculating the average gray value of the image. The initial value, $\mu^{(0)}$, divides the image into two regions, R_1 and R_2, where R_1 and R_2 denote the regions where gray values are higher and lower, respectively, than the initial value. Then, to calculate a new threshold value, the average gray values of each, $\mu_1^{(1)}$ and $\mu_2^{(1)}$, with R_1 and R_2 are calculated and the new threshold value is calculated using $\mu^{(1)} = \frac{\mu_1^{(1)} + \mu_2^{(1)}}{2}$, where the subscript indicates the region and the superscript is the calculating step. Repeating these calculations until converges, the threshold level can be obtained as:

$$\mu^{(n)} = \frac{\mu_1^{(n)} + \mu_2^{(n)}}{2} \tag{13}$$

When the iterative threshold level is applied to a dual-active contour, a single sub-domain is divided into two regions by each initial threshold level, and the iterative calculations in each sub-domain are executed until the threshold level converges. Each sub-domain consists of a line connecting the n[th] points of the inner and outer contours, as shown in Fig. 6. IS_k and OS_k denote the k[th] point on the inner and outer contours, respectively, and $G_{k,m}$ is the gray value of the k[th] sub-domain and the m[th] virtual position on the k[th] sub-domain, i.e., on the k[th] line. After all the threshold values of the sub-domain converge, Eq. (9) is modified as:

$$\vec{F}_{img}(s,t) = J_W(v(s,t))\left[J(v(s,t)) - J_C(v(s,t))\right]\left[\frac{x-x_0}{r(s,t)}, \frac{y-y_0}{r(s,t)}\right]^T \tag{14}$$

where $J_C(v(s,t)) = J_C(k) = func(G_{k,0}, G_{k,1}G_{k,2}, \cdots, G_{k,M})$ is dependent on the local position and the iterative step.

4. DESCRIPTION OF THE DEVELOPED ALGORITHM

As the first step of the developed algorithm, the bubble boundaries on each plane are extracted by applying the improved dual active contour model. Since the focal length between two images can be different, two images are linearly scaled according to length based on a common axis, i.e. the length of the z-axis in the case where the images lie on the xz- and yz-planes. After two images are scaled, some assumptions are applied to reconstruct the bubble image. It is assumed that the two images are positioned at an orthogonal plane. Therefore, one image is on the xz-plane and the other is on the yz-plane. It is further assumed that those images are silhouettes of the objects to each plane. The object of interest is considered to be that with two contact points with the planes, which are parallel to the xy-plane. The contact points are positioned at the top and bottom of the cuboids that include the object, as shown in Fig. 7-(a). The silhouettes of the xz- and yz-plane then have two points of contact with the lines, which are parallel to the x- and y-axes, respectively. Those points are positioned at the top and bottom of a rectangle including the projected images. The top and bottom points of contact with the cuboids correspond to the top and bottom, respectively, points of contact with the rectangle in the xz- and yz-planes. These descriptions are shown completely in Figs. 7-(a) and 7-(b).

At this point, the points consisting of the contour projected on the xz-plane do not have y-coordinate information, while those of the silhouette on the yz-plane do not have x-coordinate information. The y-coordinate information of the snake in the xz-plane could be obtained from the snake on the yz-plane. That is, the y-coordinate of the snake in the xz-plane becomes the y value that corresponds to the z-coordinate in a line connecting two contacting points on a line parallel with the y-axis, as shown in Fig. 7-(b). In the same manner, the x-coordinate of the snakes in the yz-plane becomes the x value that corresponds to the z-coordinate in a line connecting two contacting points on a line parallel with the x-axis, as shown in Fig. 7-(c). Therefore, four points could be found on one plane that is parallel to the xy-plane, as shown in Fig. 8. It is assumed that the

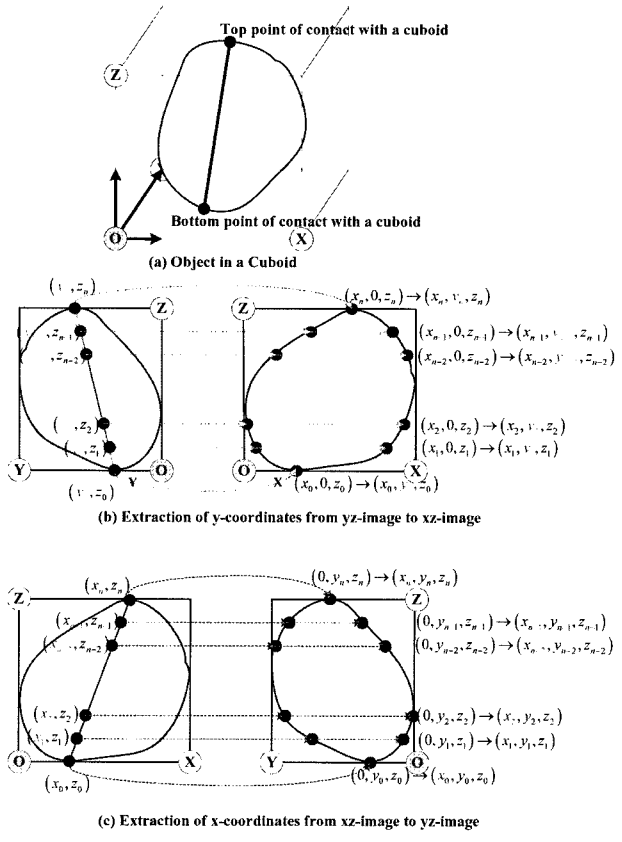

Fig. 7. Descriptions of the Developed Algorithm to Reconstruct Two Images

four points are positioned at the ellipsoidal boundary as follows:

$$\frac{(x-x_{ci})^2}{a_i^2}+\frac{(y-y_{ci})^2}{b_i^2}=1 \qquad (15)$$

The centroid of the ellipsoid can be obtained, because the two images are orthogonal, as follows:

$$C_i(x_{ci},y_{ci},z_{ci})=\left(\frac{x_0+x_1}{2},\frac{y_2+y_3}{2},z_i\right) \qquad (16)$$

Furthermore, if the arrangement of the four points found above is equivalent to that shown in Fig. 8, an inconsistency that conflicts with the assumptions may arise. That is, the points are found in the projected image, and as such they have to be positioned on the boundary and be contact points on the object. However, the boundary of the projected object based on the projected ellipse in Fig. 8 is not consistent with the originally extracted boundary, because the condition for the points to contact with the projecting plane is excluded in the arrangement of points in Fig. 8.

When the four points are positioned as given in Fig. 9 and the two assumptions are satisfied, an ellipse conditionally exists. Thus, it is assumed that the four different ellipses consist of each cross-section, as shown in Fig. 9. At this time, the four pieces of the ellipsoid have a different centroid, and major and minor axes. From these centroids, the major and minor lengths of the volume of each slice can be calculated by the following equation:

$$V_i=\left(\sum_{j=0}^{3}A_j-A_{rec,i}\right)\Delta z_i=\left(\frac{\pi}{4}\sum_{j=0}^{3}a_jb_j-A_{rec,i}\right)\Delta z_i \qquad (17)$$

where j denotes each piece of the ellipse, and a and b are the major and minor length of each ellipse, respectively. However, the rectangle connected by the four centroids is overlapped ($A_{rec,i}$), as shown in Fig. 10, and thus must be removed. The total volume is calculated by stacking each oval volume, the equivalent diameter is calculated by the calculated volume, and the surface area is calculated by stacking the meshed triangles between the two slices.

The procedures described above comprising the

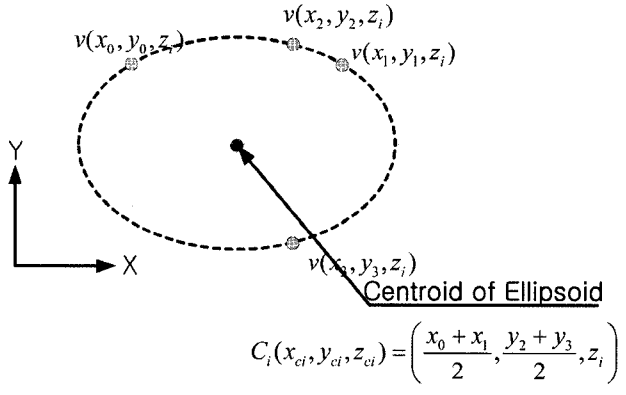

Fig. 8. Finding Ellipsoid Center at Each Plane

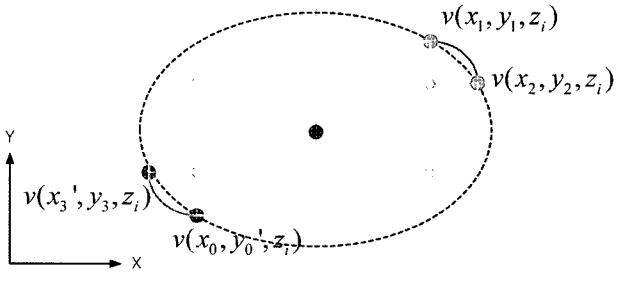

Fig. 9. Rearrangement of Points at Each Plane

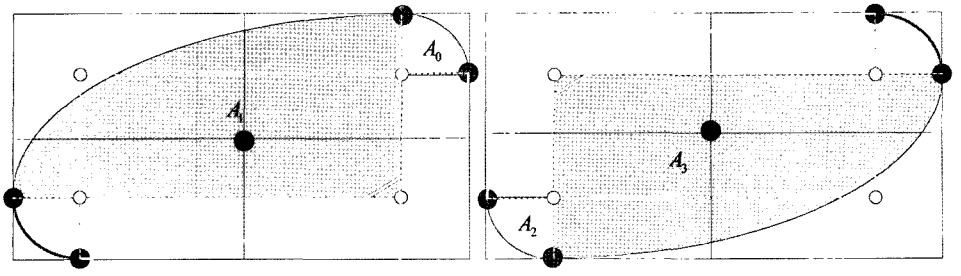

Fig. 10. Overlapping Area Among Four Pieces of Ellipsoids

developed algorithm are summarized as follows:

i. Extraction of boundaries from orthogonal images (e.g. xz- and yz-planes)
ii. Linear scaling of two extracted boundaries for the height ratio
iii. Extension of 2D points on each plane into 3D points in space
iv. Reconstruction of 3D bubble
v. Calculation of bubble volume, surface area, and diameter

5. RESULTS AND DISCUSSION

5.1 Verification of the Developed Algorithm

5.1.1 Improved Central Contour Model

The improved boundary extraction procedure using the central-active contour model proposed in the present study was compared with an existing model and verified by testing an image with a trivial boundary. The test results are summarized in Fig 11. The 1st and 3rd rows show the initial state of the contour and the results of extracting the boundary using the original and proposed models, as well as the dual-active contour model are depicted in Fig 11. The inner and outer points indicate the outer and inner contours, respectively. The improved model in this study is tested for three cases. Case (a), which corresponds with case (d), is the simple case of a black circle in a white background. This case was selected to check whether the proposed model inherits the characteristics of the single-active contour model, whose threshold value is a constant, as in Eq. (9). From the results of applying the proposed model to this case, it is found that the proposed model can extract the same boundary as the original central contour model.

In case (b), which corresponds with case (e), the gray level of the boundary between the object of interest and the surroundings varies. The object of case (b) is generated by filling a regular octahedron with the gray level, which increases from 30 to 240 in a counterclockwise direction. Thus, only one piece among the eight regions in the regular octahedron is found if a constant value is employed for the threshold level when the reference point is positioned in the region of interest. However, the original model extracted the boundary incorrectly, as shown Fig. 11. Since the proposed model uses local threshold levels that are updated at every iteration, the calculated boundary agrees with the actual boundary, and thus it is demonstrated that the proposed model successfully extracted the boundary, as shown in Fig. 11-(e). The boundaries of cases (b) and

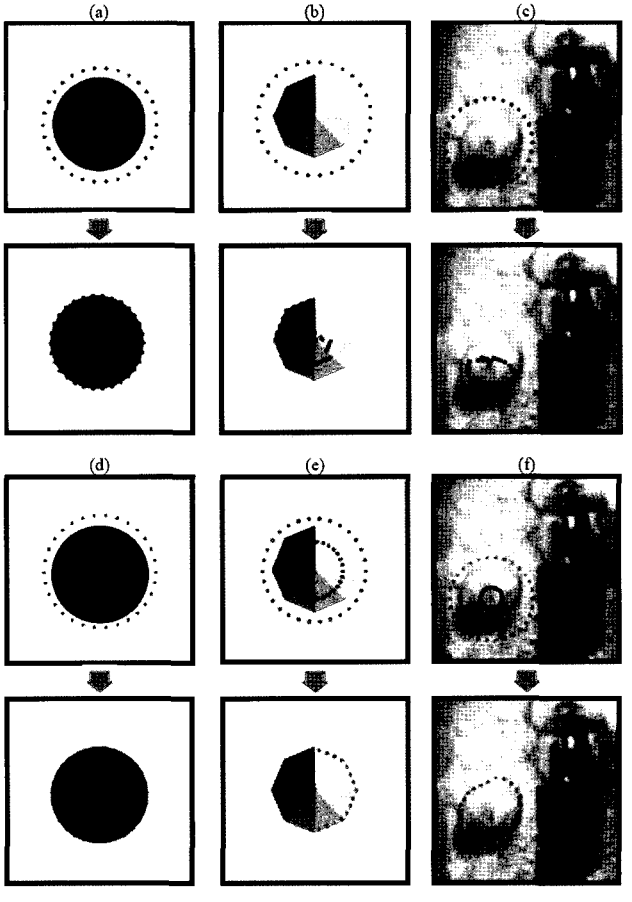

Fig. 11. Results of Proposed Dual Active Contour Model Applying the Iterative Threshold Method
(a, b, c: Original Model d, e, f: Improved Model)

(e) are distinct, and the gray level of the background is uniformly white. Thus, it is apparent that objects having an obscure boundary and edge, such as the bubbles shown in Fig. 2, require application of the proposed model. An actual bubble was selected for case (c), which corresponds with case (f), and the bubble is positioned at the left lower corner, as shown in Fig. 2. It is difficult to extract the bubble from the background using the original central contour model, even though the boundary of the bubble can be distinguished by the naked eye. This explains why the gray levels on the bubble boundary are not constant and there are various gray levels of the background. When the improved central contour model is applied to this bubble, the boundary is successfully extracted, as shown Fig. 11-(f). From these results, it is demonstrated that the proposed model can be applied even to boundary extraction problems involving an obscure boundary and a non-uniform background.

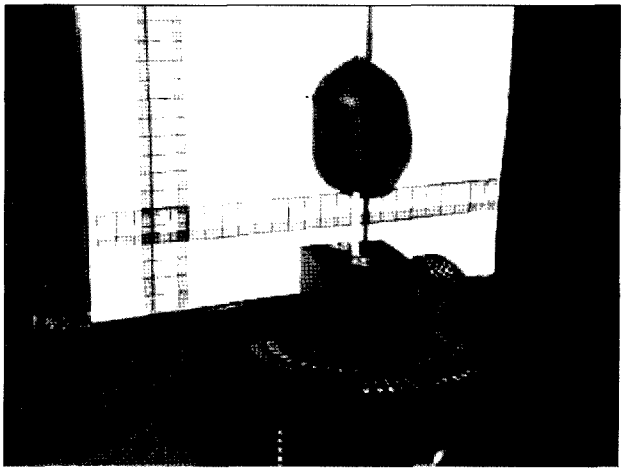

Fig. 12. Experimental Facility to Record Revolving Objects

5.1.2 Qualitative Confirmation of Reconstructed Object

An experiment was conducted to confirm the capacity of the developed algorithm to reconstruct three-dimensional objects. Figure 12 shows a traversing unit with the ability to rotate an object from 0 ° to 180 °. The objects were made from rubber clay and are supported by a white stick having the same color as the background in order to obtain a chroma-key effect. The images were obtained when the traversing unit moved in 15 ° increments in the counter-clockwise direction. The three objects were tested and the results are summarized in Fig. 13. In all cases, two images taken when the object was rotated by 0 ° and 90 ° were used to reconstruct the 3D shape using the algorithm developed in this study. The boundaries were extracted for each image and these boundaries were merged using the developed algorithm. The reconstruction results for the actual objects are presented in Fig. 13. In all cases, the reconstruction was very successful. From the results, it was that the shapes of the reconstructed object were

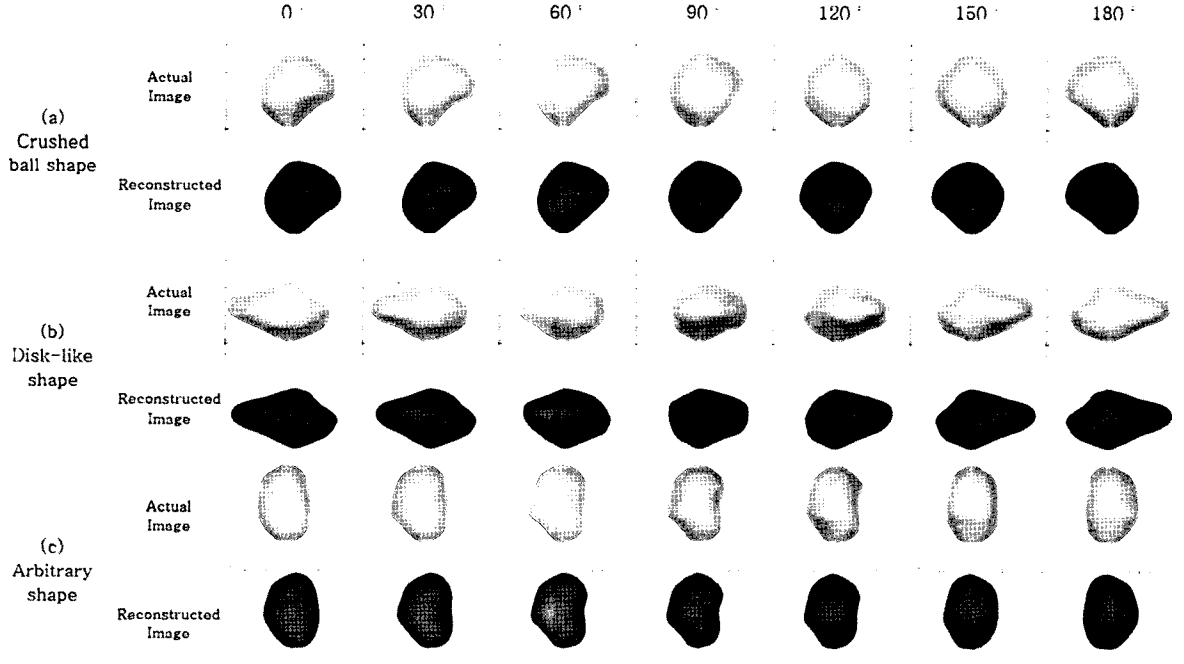

Fig. 13. Comparison of Actual Object and Reconstructed Object

similar or almost identical with those of the real object at most of the rotated angles. Thus, the results confirm that the objects reconstructed from the developed algorithm can reveal the characteristics of the real objects, even though only two orthogonal images are used. However, the reconstructed results could be affected by selecting two images, as only two orthogonal images are used in the case of an axis-unsymmetrical object. Images photographed using a recording device, such as condensing bubble images in subcooled boiling, are arbitrary with respect to angle in real applications. As such, the reconstructed results require a sensitivity analysis for selecting two images with rotated angles. The results of the sensitivity analysis are summarized in Table 2. Two images to reconstruct object are selected at 15 ° increments in the counterclockwise direction. Thus, for example, if one of the images is at 15 °, the other image is at 105 °. From the results of this analysis, it is shown that the developed algorithm can reconstruct the objects within ±4 % error even if the selected orthogonal double images are changed, as shown in Table 2.

5.1.3 Quantitative confirmation of reconstructed object

The algorithm developed to calculate the bubble surface area, volume, and equivalent diameter from two orthogonal images is verified by simulating generated images using a CAD program, AutoCAD 2002 software. The three-dimensional objects are created through AutoCAD and orthogonal images are obtained from the generated objects. The actual information of the generated objects such as their volume and surface area is acquired from AutoCAD's internal calculator. The information from AutoCAD is used as reference values. The generated images and the reconstructed images of the calculated results are depicted in Fig. 14. The differences in volume and surface area between the generated

Table 2. Sensitivity Analysis with Selection of Two Orthogonal Images

		Volume (mm^3)			Area (mm^2)		
XZ	YZ	Crushed ball shape	Disk-like shape	Arbitrary shape	Crushed ball shape	Disk-like shape	Arbitrary shape
0 °	90 °	8367.00	9865.94	13140.40	2066.43	2514.27	2820.27
15 °	105 °	8219.08	9377.18	13399.32	2041.96	2554.37	2854.67
30 °	120 °	8046.48	9747.88	13363.48	2016.16	2536.64	2845.81
45 °	135 °	8131.85	9626.22	13117.79	2029.20	2461.35	2801.03
60 °	150 °	8050.26	9574.41	12780.34	2056.00	2414.46	2764.95
75 °	165 °	8116.41	9249.98	12556.42	2070.40	2341.85	2749.23
Average		8155.18	9573.60	13059.63	2046.69	2470.49	2805.99
Standard deviation		121.51	228.87	331.31	21.44	81.36	42.64
CV(coefficient of variation)		0.0149	0.0239	0.0254	0.0105	0.0329	0.0152

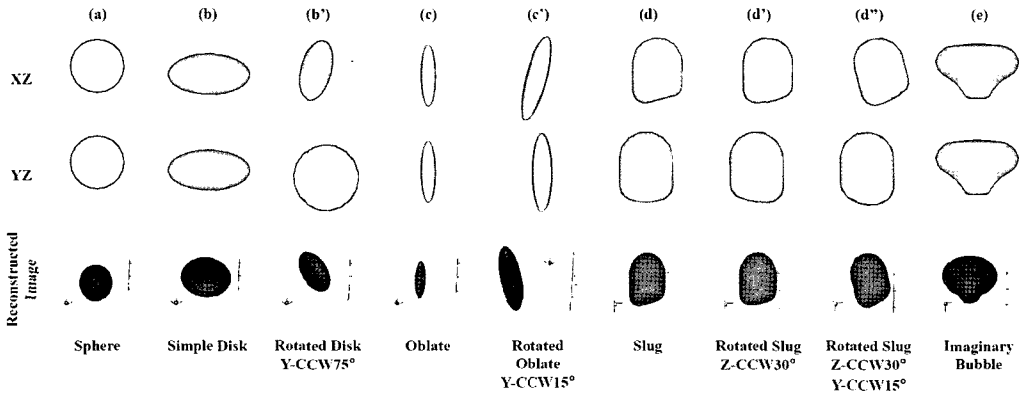

Fig. 14. Calculated Matrix and Reconstructed Results

Table 3. Results of the Calculated Volume and Area Using the Developed Algorithm

Case		Volume Error (%)	Area Error (%)
(a)	Sphere	3.61	2.27
(b)	Simple disk	-0.27	0.28
(b')	Rotated disk (Y-CCW 75)	-4.59	-3.66
(c)	Oblate	5.78	3.71
(c')	Rotated oblate (Y-CCW 15)	4.08	2.45
(d)	Slug	-1.17	-0.64
(d')	Rotated slug (Z-CCW 30)	5.08	0.66
(d'')	Rotated slug (Z-CCW 30 & Y-CCW 15)	-0.46	-1.39
(e)	Imaginary bubble	3.93	1.91

and reconstructed images are summarized in Table. 3. In Table 3, Y and Z denote the rotational axes, which are the x- and z-axes. CCW denotes the counterclockwise direction. Thus, in case (b') the object is rotated as in case (b) on the y-axis by 75 degrees counterclockwise. In the same manner, the rotated oblate of case (c') rotates the oblate of case (c) on the y-axis by 15 degrees counterclockwise. The object of case (d'') is rotated twice, i.e., on the z- and y-axis. The results calculated using the algorithm are tabulated in Table 3. From the results, it is shown that the developed algorithm can estimate the volume and area of objects within ±6 % and ±4 % error, respectively.

5.2 Application of Condensing Bubble in a Subcooled Boiling Flow

The developed algorithm was applied to actual bubble images in a subcooled boiling flow. Bubbles generated in a heated wall condensed in the subcooled liquid at the center of the flow. The images were sequentially recorded by a high-speed camera, as shown in Fig. 15. The bubble boundaries extracted using the improved dual active contour model, shown in Fig. 15, confirm that the boundaries are precisely found. The images in the left and right columns of images (a) are used as images on the xz- and yz-planes, respectively. The images between the left and right columns of images (a) are orthogonal and the positions of the recording camera are fixed. The reconstructed three-dimensional bubble images are shown in Fig. 15-(c). Good results are obtained when the developed algorithm is used to measure the actual vapor bubbles. Thus, it can be concluded that the developed algorithm can be used to analyze the characteristics of vapor bubbles in a subcooled boiling flow. It is expected that the variables calculated from the images reconstructed using the algorithm, i.e., volume, surface area, equivalent diameter, and interfacial area concentration, are estimated more accurately than those measured using a single directional image. These variables are presented in Table 4. Furthermore, it is expected

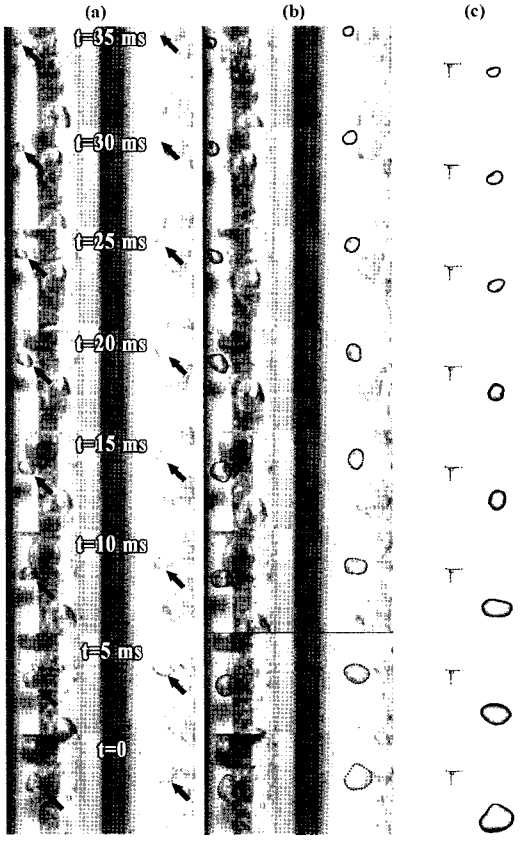

Fig.15. Reconstruction of Condensing Bubble in Subcooled Boiling
(a) - Recorded Images, (b) - Extracted Bubble Boundaries, (c) - Reconstructed Bubble Images

that the three-dimensional motions of the bubble can be observed by its sequential reconstruction using the developed algorithm, as shown in Fig. 16.

Comparisons between the orthogonal two image

Table 4. Results of the Condensing Bubble (Volume, Area, Diameter, Etc.)

Time (ms)	Volume (mm^3)	Area (mm^2)	Volume Equivalent Diameter (mm)	Sauter Diameter (mm)	Bubble Velocity (m/s)	Condensing Rate (m^3/s)
0	60.7306	77.4657	4.8768	4.7038	0.1987	3999.3700
5	40.7337	58.9573	4.2689	4.1454	0.2473	1223.1940
10	34.6178	54.4218	4.0436	3.8166	0.2050	2454.9080
15	22.3432	39.6874	3.4945	3.3779	0.2858	1108.6020
20	16.8002	33.7079	3.1776	2.9904	0.2455	1622.9768
25	8.6853	21.4855	2.5503	2.4254	0.2714	5.7538
30	8.6566	20.9393	2.5475	2.4805	0.1865	819.4766
35	4.5592	14.7634	2.0573	1.8529		

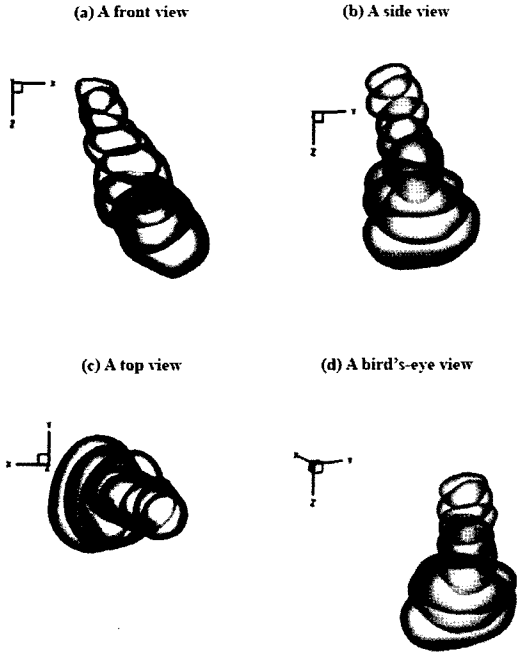

Fig. 16. Sequences of Reconstructed-Bubble Motion Over Time

processing approach and single image processing for identical bubbles were carried out by calculating bubble volume and surface area. The results are summarized in Table 5. The results listed in Table 5 show the condensed bubble of interest. The left and right bubbles indicated by the arrow are recorded on the front and side of the heated wall, respectively. In the case of the two orthogonal image processing approach, two images are used to calculate the bubble volume. However, only one image on the side view is used to calculate the bubble volume in the case of singe image processing. Thus, it is assumed that the bubble is a revolving solid, i.e., oblate or prolate with a circular cross-section. At this point, the revolving axis becomes the nearest axis to an axial direction. In cases (a) and (b), i.e., bubbles similar to a revolving solid, the results obtained by applying single image processing agree well with those where two orthogonal image processing is applied. However, the obtained volume and surface area in the case of single image processing are inaccurate when there are bubble deformations from the revolving shape. In particular, when the bubble shape on the front view is larger than that on the side view, the single image processing overestimated the bubble volume and surface area, as shown in Table 5, cases (c) and (d). On the contrary, the single image processing underestimated the bubble volume and surface area when the bubble shape on the front view is smaller than that of the side view, as shown in Table 5, cases (e) and (f). This indicates that single image processing has limitations when applied to deformable bubbles in subcooled boiling. It should be noted that a more realistic shape can be obtained when the developed algorithm is used.

The developed algorithm can be applied to the reconstruction of three-dimensional bubble shape without a concave surface as for a common axis of two image planes even though the void fraction is high. Thus, the proposed algorithm can be applicable when there are coalescence and breakup of bubbles without concave surface.

6. CONCLUSIONS

An algorithm was developed to reconstruct two orthogonal images into a three-dimensional image. To extract the boundary of an obscure object with a non-uniform background gray level tone, a modified model was proposed. The model proposed in this study is a

Table 5. Comparison Between Two Orthogonal Image and Single Image Processing Approaches

Case	Image Processing	Volume (mm^3)	Surface Area (mm^2)	Photographs Left bubble: front view Right bubble: side view
(a)	Double	7.509	18.912	
	Single	7.496	18.527	
	Ratio	1.001	1.021	
	Description	Similar	Similar	
(b)	Double	31.257	48.661	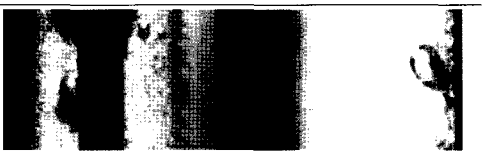
	Single	32.165	49.010	
	Ratio	0.972	0.993	
	Description	Similar	Similar	
(c)	Double	48.324	71.491	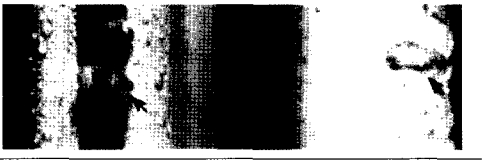
	Single	39.155	62.891	
	Ratio	1.234	1.137	
	Description	Underestimated	Underestimated	
(d)	Double	62.677	82.959	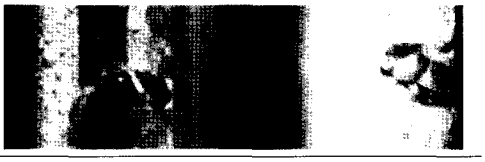
	Single	44.539	61.126	
	Ratio	1.407	1.357	
	Description	Underestimated	Underestimated	
(e)	Double	26.837	45.895	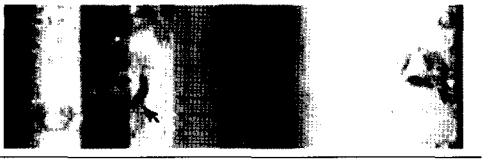
	Single	39.264	56.046	
	Ratio	0.684	0.819	
	Description	Overestimated	Overestimated	
(f)	Double	91.581	102.300	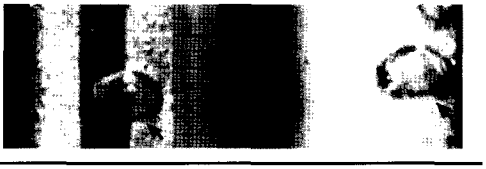
	Single	141.885	135.140	
	Ratio	0.645	0.757	
	Description	Overestimated	Overestimated	

dual-active contour model based on a modification to the image function on the central-active contour model. The accuracy of the proposed model and the developed algorithm was verified through a simulation of imaginary images and by experiments. The boundary of the obscure object was easily found by applying the dynamic threshold value of the proposed model. Reconstruction with the developed algorithm was confirmed to be very successful. The results of the simulations and experiments showed that volume and surface area calculated with the algorithm exhibited better agreement with the actual values than did the measured values obtained using a single-directional image. Furthermore, three-dimensional images were obtained successfully from experimental application of the developed algorithm to a condensed bubble in a subcooled boiling flow. It is expected that further analysis of images reconstructed by the developed algorithm will produce even more accurate bubble parameters such as equivalent diameter and surface area.

NOMENCLATURE

A	triangle area ($pixel^2$)
A_{rec}	rectangular area ($pixel^2$)
a	x-directional axis length of ellipse (pixels)
b	y-directional axis length of ellipse (pixels)
E	energy (J)
F	force (N)
h_1	energy function coefficient 1
h_2	energy function coefficient 2

IS inner snake (inner contour)
J image contrast
J_c threshold brightness value
J_w the coefficient defining the magnitude and direction of image force
m mass density (kg/m^3)
N number of points
OS outer snake (outer contour)
R_1 the region where gray values are higher
R_2 the region where gray values are lower
r distance (pixels)
s parameter variable
u_x x directional ratios between the considered point and the near integer lattice point
u_y y directional ratios between the considered point and the near integer lattice point
W_1 resistance to stretching
W_2 resistance to bending
x x – coordinate (pixels)
x_0 x – coordinate of reference point (pixels)
y y – coordinate (pixels)
y_0 y – coordinate of reference point (pixels)
z z – coordinate (pixels)

Greek Letters

γ damping viscosity factor
μ threshold value

Subscripts

ext external
i ith position
int internal
img image
rig rigidity
tens tension

REFERENCES

[1] Situ, R., Mi, Y., Ishii, M., Mori, M., "Photographic Study of Bubble Behaviors in Forced Convection Subcooled Boiling," International Journal of Heat and Mass Transfer, Vol. 47, pp. 3659-3667, (2004).
[2] Maurus, R., Ilchenko, V., Sattelmayer, T., "Automated High-Speed Video Analysis of the Bubble Dynamics in Subcooled Flow Boiling," International Journal of Heat and Fluid Flow, Vol. 25, pp. 149-158, (2004).
[3] Zeitoun, O., Shoukri, M., Chatoorgoon, V., "Measurement of Interfacial Area Concentration in Subcooled Liquid-vapor Flow," Nuclear Engineering and Design, Vol. 152, pp. 243-255, (1994).
[4] Hibiki, T., Hazuku, T., Takamasa, T., Ishii, M., "Some Characteristics of Developing Bubbly Flow in a Vertical Mini Pipe," International Journal of Heat and Fluid Flow, (2007).
[5] Takamasa, T., Goto, T., Hibiki, T., Ishii, M., "Experimental Study of Interfacial Area Transport of Bubbly Flow in Small -Diameter Tube," International Journal of Multiphase Flow, Vol. 29, pp. 395-409, (2003).
[6] Takamasa, T., Watarai, M., "Measurement of Bubble Interfacial Configurations in Vertical Bubbly Flow Using Stereo Image-Processing Method (SIM)," In: Proceedings of ASME Fluids Engineering Division Summer Meeting, FED-239, Vol. 4, pp. 175-180, (1996).
[7] Davis, S., "A Survey of Edge Detection Techniques," CGIP, Vol. 4, pp. 248-270, (1975).
[8] Marr and Hildreth, E., "Theory of Edge Detection," Proceedings of the Royal Society, B-207, pp. 187-217, (1980).
[9] Canny, J., "A Computational Approach to Edge Detection," IEEE Trans. PAMI, Vol. 8, No. 6, pp. 697-698, (1986).
[10] Kass, M., Witkin, A., Terauzopoulos, D., "Snake : Active Contour Models," International Journal of Computer Vision, Vol. 1, No. 4, pp. 321-331, (1988).
[11] Tsai, C. T., Sun, Y. N., Chung, P. C., "Minimizing the Energy of Active Contour Model using Hopfield Network," IEE Proceedings-E, Vol. 140, No. 6, pp. 297-303, (1993).
[12] Lam, K. M., Yan, H., "Fast Greedy Algorithm for Active Contours," Electronic Letters, January, Vol. 30, No. 1, pp. 21-23, (1994).
[13] Szczypiński, P. and Strumiłło, P., "Application of an Active Contour Model for Extraction of Fuzzy and Broken Image Edges," Machine GRAPHICS & VISION, Vol. 5, No. 4, pp. 579-594, (1996).
[14] Gunn, S. R. and Nixon, M. S., "A model based dual active contour," In E. Hancock, editor, Proc. British Machine Vision Conference, pp. 305–314, York, U.K., 1994. BMVA Press.